

Exciton Mott transition revisited

Daniele Guerzi,¹ Massimo Capone,¹ and Michele Fabrizio¹

¹*International School for Advanced Studies (SISSA), Via Bonomea 265, I-34136 Trieste, Italy*

(Dated: January 9, 2023)

The dissociation of excitons into holes and electrons in photoexcited semiconductors, despite being one of the first recognized examples of a Mott transition, still defies a complete understanding, especially regarding the character of the transition, which is first order in some cases and second order in others. Here we consider an idealized model of photoexcited semiconductors that can be mapped onto a spin-polarised half-filled Hubbard model, whose phase diagram reproduces most of the phenomenology of photoexcited semiconductors and uncovers the key role of the exciton binding energy in determining the order of the exciton Mott transition.

The transition between an exciton gas and an electron-hole liquid (EHL) in photoexcited semiconductors (PES) above the exciton condensation temperature is since long known [1–3] to realise an almost ideal Mott transition [4], i.e., a metal-insulator transition driven by interaction and not accompanied by any symmetry breaking. Nevertheless and despite the great progresses in the theoretical understanding of the Mott transition, several aspects remain puzzling, in the first place the nature of the transition, which in many experiments looks first-order [5–8], in agreement with Mott’s prediction [4], while in many others seems rather a continuous transition [9–12]. In view of the revived interest in the physics of excitons stimulated by the unique properties of transition metal dichalcogenides [13], the solution of this basic yet open issue in the exciton Mott transition cannot be further delayed. The scope of the present work is just putting together some pieces of that puzzle.

Important insights into the physics of Mott transitions have been provided in the last decades by dynamical mean field theory (DMFT) [14]. According to DMFT, which is strictly exact only in lattices with infinite coordination number, the spectral function of the correlated metal just before the Mott transition displays simultaneously low-energy quasiparticles, narrowly peaked at the chemical potential, and high-energy precursors of the Hubbard sidebands. This dual nature is closely related to a metal-insulator coexistence in a whole range of Hamiltonian parameters [15] that leads to a finite-temperature first-order Mott transition.

Such inherently first-order nature of the Mott transition uncovered by DMFT confirms the original prediction by Sir Nevill Mott [4], even though the original arguments emphasised the role of the long-range Coulomb interaction in binding holes to electrons, while in DMFT one usually considers only the short-range part of that interaction, parametrised by the on-site Hubbard U . A connection between the two viewpoints can nevertheless be built in the context of PES. In this perspective, we shall consider an idealised modelling of these systems. In order to single out the interaction physics, we neglect

the effective mass difference between valence and conduction bands, as well as the spin and eventually the valley degrees of freedom. We can then map the conduction and valence electrons into effective spin-up and spin-down fermions, respectively, so that the Coulomb interaction becomes an attractive pairing potential. If the latter is further approximated by an on-site attraction $-U < 0$, and the bands by those of a tight-binding Hamiltonian with nearest-neighbour hopping, the model becomes an attractive Hubbard model at fixed electron density [16] $n = \langle n_{i\uparrow} \rangle + \langle n_{i\downarrow} \rangle = 2\langle n_{i\uparrow} \rangle$, where $n/2 \ll 1$ corresponds to the number of photoexcited electron-hole pairs. We emphasise that the analogy holds only if U is large enough to create bound states below the two-particle continuum, which play the role of the excitons in the original system.

If, in addition, the lattice is assumed to be bipartite, upon the particle-hole transformation $d_{i\uparrow} \rightarrow \pm d_{i\uparrow}^\dagger$, where the \pm sign refers to the two different sublattices and $d_{i\sigma}^\dagger$ creates a spin- σ electron at site i , the attractive Hubbard model transforms into the half-filled repulsive model

$$H = -\frac{t}{\sqrt{z}} \sum_{\langle ij \rangle} \sum_{\sigma=\uparrow,\downarrow} \left(d_{i\sigma}^\dagger d_{j\sigma} + H.c. \right) + U \sum_i n_{i\uparrow} n_{i\downarrow} - h \sum_i (n_{i\uparrow} - n_{i\downarrow}), \quad (1)$$

where z is the coordination number and the magnetic field h must be fixed by imposing that the magnetisation $m = \langle n_{i\uparrow} \rangle - \langle n_{i\downarrow} \rangle = 1 - n$, being $n_{i\sigma} = d_{i\sigma}^\dagger d_{i\sigma}$.

In short, the physics of PES can be captured by the half-filled repulsive Hubbard model at fixed – large if $n \ll 1$ – magnetisation, provided all assumptions above are valid. Indeed, the Hamiltonian (1) is expected to display several phases in one to one correspondence to those of PES: a low-temperature canted antiferromagnetic insulator, which translates into a phase of condensed excitons, and high temperature paramagnetic Mott insulating and metallic phases, which correspond to the so-called exciton Mott insulator and EHL, respectively.

We are particularly interested in the high-temperature phases and the transition between them, which can be inferred from ground-state calculations of (1) if we force

the translational and residual spin- $U(1)$ symmetries, on the proviso that preventing symmetry breaking in a ground-state calculation correctly reproduces the system above the critical temperature.

Despite the impressive advances in numerical methods for solving DMFT, the phase diagram of the simple half-filled repulsive Hubbard model in a Zeeman field is still controversial. The Hamiltonian (1) was studied by DMFT not allowing for antiferromagnetism in Refs. [17], [18] and [19], using different impurity solvers: exact diagonalisation at finite [17] or zero [18] temperature, and numerical renormalisation group [19]. The phase diagrams that were obtained look superficially similar. In particular, in the large $U \gg h$ regime pertinent to PES, the Mott transition was found to be always discontinuous, in contrast with experiments in PES where both first- and second-order transitions are observed.

Moreover, the previous calculations disagree on the physical properties across the transition. Specifically, according to [17] and [18] the transition separates a partially polarised metal from a partially polarised insulator. By contrast, the partially polarised insulator has not been found in Ref. [19] that instead reports a transition between a partially polarised metal and a fully polarised insulator.

The reason of this discordance can be readily traced back. Within DMFT the lattice model is mapped onto an Anderson impurity model (AIM) with the conduction bath determined self-consistently [20]. In particular, the Mott insulator maps onto an AIM with a hybridisation spectrum that has a gap of order U at the chemical potential. Consequently, the ground state of the AIM has spin $1/2$, mostly localised on the impurity, and is separated by a finite gap $\sim U$ from the lowest excited state. An impurity Zeeman field splits linearly the ground-state spin degeneracy, and is therefore unable to stabilise a pure state with a continuously varying impurity magnetisation [21], which translates into the spin-polarisation m of the lattice model. This explains why a straight $T = 0$ calculation as in [19] is not able to converge to a partially polarised Mott insulator, as we indeed checked [22]. The same difficulty does not arise if one searches for a mixed state, as in [17] and [18], though this choice can force the stabilisation of an artificial solution.

To settle this issue we decided to resort to a recently developed approach [23], which extends the conventional Gutzwiller variational wavefunction and has been named *ghost* Gutzwiller wavefunction (g-GW), i.e.,

$$|\Psi\rangle = \prod_i \mathcal{P}_i |\Psi_*\rangle, \quad (2)$$

where $|\Psi_*\rangle$ is a Slater determinant, ground state of a tight-binding variational Hamiltonian H_* for $N \geq 1$ spin-

ful orbitals, while

$$\mathcal{P}_i = \sum_{\Gamma\gamma} \lambda_{\Gamma\gamma} |\Gamma_i\rangle \langle \gamma_i|, \quad (3)$$

is a linear operator at site i , where $|\Gamma_i\rangle \langle \gamma_i|$ projects a local N -orbital configuration $|\gamma_i\rangle$ into a physical single-orbital one $|\Gamma_i\rangle$, and $\lambda_{\Gamma\gamma}$ are variational parameters. The trick of adding subsidiary degrees of freedom to improve the accuracy of a variational wavefunction has a long history that goes back to the shadow wavefunctions for ^4He [24], and is still very alive, as testified by the great interest in matrix-product states and tensor networks [25, 26], or, more recently, in neural-network quantum states [27]. The wavefunction (2) is simple, it gives the possibility to calculate analytically expectation values in infinite-coordination lattices [23], and, moreover, it bears close similarity to DMFT. Indeed, as noted in [28], the variational parameters $\lambda_{\Gamma\gamma}$ can be associated to the components $\psi(\Gamma, \bar{\gamma})$, where $|\bar{\gamma}\rangle$ is the particle-hole transform of $|\gamma\rangle$, of a wavefunction $|\psi\rangle = \sum_{\Gamma\bar{\gamma}} \psi(\Gamma, \bar{\gamma}) |\Gamma\rangle \times |\bar{\gamma}\rangle$ that describes an impurity coupled to a bath of N levels. The analogy with DMFT is now self-evident.

We apply the g-GW approach to study the model (1) on a Bethe lattice with coordination number $z \rightarrow \infty$. We refer to the original work [23], see also [22, 28], for more details. We choose to work with $N = 3$ subsidiary orbitals, with creation operators $c_{i a \sigma}^\dagger$, $a = 1, \dots, 3$, which was shown [23] to provide already very accurate ground state properties in comparison with DMFT. Moreover, we treat all components $\psi(\Gamma, \bar{\gamma})$ of the wavefunction describing a quantum impurity coupled to a bath of $N = 3$ levels as free variational parameters, apart from normalisation and the constraints due to spin- $U(1)$ and particle-hole symmetries. This means that, in contrast with the original work [23], we do not require $\psi(\Gamma, \bar{\gamma})$ to be ground state of an auxiliary Anderson impurity model, i.e., an interacting impurity hybridised with a non-interacting bath, an unnecessary requirement which would lead to the same problems of the DMFT solution.

In the limit $z \rightarrow \infty$, the expectation value per site E of the Hamiltonian (1) at $h = 0$ on the variational wavefunction (2) at fixed spin-polarisation m can be written as a functional of ψ only, and reads [23]

$$E[\psi] = \frac{1}{V} \langle \Psi_* | H_* | \Psi_* \rangle + U \langle \psi | n_\uparrow n_\downarrow | \psi \rangle, \quad (4)$$

where V is the number of sites, and n_σ the spin- σ occupation number of the impurity. The Slater determinant Ψ_* is the ground state of the non-interacting Hamiltonian

$$H_* = -\frac{t}{\sqrt{z}} \sum_{a,b=1}^3 \sum_{\langle ij \rangle \sigma} \left(R_{a\sigma}^* R_{b\sigma} c_{i a \sigma}^\dagger c_{i b \sigma} + H.c. \right) - \sum_{i\sigma} \sum_{a,b=1}^3 \left(\mu_{ab\sigma} (c_{i a \sigma}^\dagger c_{i b \sigma} - \Delta_{ab}) + H.c. \right). \quad (5)$$

The Lagrange multipliers $\mu_{ab\sigma}$ in (5) enforce the constraint [23]

$$\langle \Psi_* | c_{i a \sigma}^\dagger c_{i b \sigma} | \Psi_* \rangle = \Delta_{ab\sigma} \equiv \langle \psi | c_{a\sigma} c_{b\sigma}^\dagger | \psi \rangle, \quad (6)$$

with the operators on the r.h.s. referring to the three levels of the bath, while the parameters $R_{a\sigma}$, regarded as components of a vector \mathbf{R}_σ , are obtained by solving

$$\mathbf{Q}_\sigma = \hat{S}_\sigma \mathbf{R}_\sigma, \quad (7)$$

where \mathbf{Q}_σ has components $Q_{a\sigma} = \langle \psi | c_{a\sigma}^\dagger d_\sigma | \psi \rangle$, and thus quantifies how much the impurity is hybridised with the bath levels, while the matrix $\hat{S}_\sigma = \sqrt{\hat{\Delta}_\sigma (1 - \hat{\Delta}_\sigma)}$, where $\hat{\Delta}_\sigma$ has the elements $\Delta_{ab\sigma}$ of Eq. (6). The energy functional $E[\psi]$ in (4) must be minimised with respect to ψ subject to the constraints fixing the density to 1 and m to the desired value, i.e.,

$$\langle \psi | n_\uparrow + n_\downarrow | \psi \rangle = 1, \quad \langle \psi | n_\uparrow - n_\downarrow | \psi \rangle = m. \quad (8)$$

Before presenting our results, we briefly mention how the Mott transition in the absence of a magnetic field occurs within this variational scheme [22, 23], which already suggests how to overcome the aforementioned problems with DMFT. Two bath levels represent the Hubbard sidebands (1 the upper and 3 the lower), while level 2 is at the Fermi level. Approaching the Mott transition from the metal side $R_{1\sigma} = R_{3\sigma} \rightarrow 1/\sqrt{2}$ and $R_{2\sigma} \rightarrow 0$ [22, 23]. Just as in DMFT, the Mott transition is signalled by the vanishing hybridisation between the impurity and the bath level at the Fermi energy. In the insulating phase, the wavefunction $|\psi\rangle$ thus factorises into a spin-1/2 wavefunction $|\phi_\sigma\rangle$ for the impurity plus sites 1 and 3, and a spin-1/2 wavefunction $|\varphi_\sigma\rangle$ of the decoupled singly-occupied level 2. However, because of equations (6) and (7), both of which determine the Hamiltonian H_* in (5) and thus its ground state, the variational wavefunction with lowest energy is actually the singlet combination $|\psi\rangle = (|\phi_\uparrow\rangle \times |\varphi_\downarrow\rangle - |\phi_\downarrow\rangle \times |\varphi_\uparrow\rangle) / \sqrt{2}$, lying $\sim J/8 = t^2/2U$ below the triplet state. In other words, despite level 2 is not hybridised with the impurity, it remains entangled with the latter in the optimised wavefunction, as clearly shown in the bottom panel of Fig. 1, where we plot, as a function of U in a region around the Mott transition, the expectation value $\langle \psi | \mathbf{S} \cdot \mathbf{S}_2 | \psi \rangle$, where \mathbf{S} and \mathbf{S}_2 are the spin operators of the impurity and the level 2, respectively. We note that this quantity is continuous across the Mott transition and approaches the spin-singlet limit $-3/4$ at large U .

The above result naturally suggests how to construct a good trial insulating wavefunction with fixed impurity magnetisation m : $|\psi\rangle = \cos\theta |\phi_\uparrow\rangle \times |\varphi_\downarrow\rangle - \sin\theta |\phi_\downarrow\rangle \times |\varphi_\uparrow\rangle$, with $\cos 2\theta \simeq m$. This wavefunction is evidently not the ground state of an Anderson impurity model. We observe that the reduced density matrix tracing out level 2, i.e., $\rho = \cos^2\theta |\phi_\uparrow\rangle \langle \phi_\uparrow| + \sin^2\theta |\phi_\downarrow\rangle \langle \phi_\downarrow|$, looks like the thermal

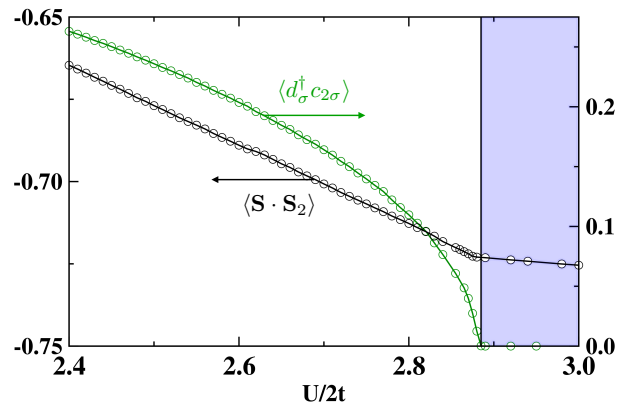


FIG. 1: Expectation value $\langle \psi | \mathbf{S} \cdot \mathbf{S}_2 | \psi \rangle$ of the spin correlation between the impurity and the level 2. Note that $\langle \psi | \mathbf{S} \cdot \mathbf{S}_2 | \psi \rangle$ increases in absolute value with $U/2t$, and is continuous across the Mott transition, despite the vanishing expectation value $\langle \psi | d_\sigma^\dagger c_{2\sigma} | \psi \rangle$ of the hybridisation, also shown.

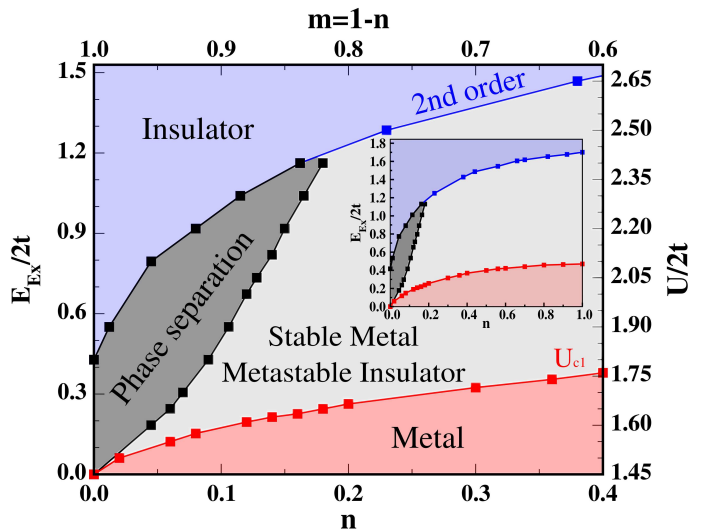


FIG. 2: Phase diagram exciton binding energy E_{ex} versus density n of photoexcited carriers, left y and bottom x axes, respectively, or, equivalently, $U/2t$ versus spin-polarisation $m = 1 - n$, right y and top x axes, respectively. In red we plot the insulator spinodal line, while in blue the metal one, which also corresponds to a second order Mott transition line. In the light grey region the stable metal coexists with a metastable Mott insulator, whereas in the dark grey area there is phase separation.

one of an Anderson impurity model in a magnetic field h , as in Ref. [17], albeit here both temperature and h are fictitious and are only used to fix the magnetisation.

The results obtained using the above wavefunction are summarized in Fig. 2, where we draw the full phase diagram U vs. m of the Hamiltonian (1), which can be translated into the phase diagram of a model for PES in terms

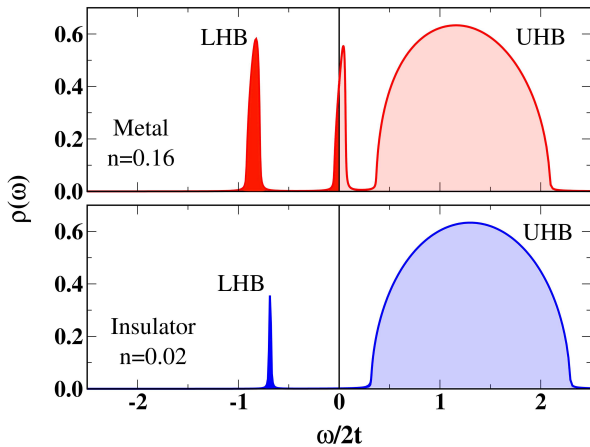


FIG. 3: Top: spectral density of the metallic solution for $U/2t = 2.2$ and density $n = 0.16$. Bottom: same quantity for the Mott insulator at the same $U/2t = 2.2$ but smaller $n = 0.02$.

of the exciton binding energy, E_{ex} defined below, and the carrier density $n = 1 - m$. As we mentioned, the correspondence holds only when excitonic bound states appear below the continuum, which happens for $U > U_{\text{cl}}(n)$, where $U_{\text{cl}}(n)$ is actually the spinodal line of the Mott insulator [15] (red curve in Fig. 2). In the light grey region above $U_{\text{cl}}(n)$ there is coexistence between a stable metal and a metastable insulator. In Fig. 3 we compare the density of states of representative metallic (top) and insulating (bottom) solutions. In the insulator we note strongly particle-hole asymmetric Hubbard sidebands, with the lower accommodating the $n \ll 1$ density of electrons. The limit $n \rightarrow 0$ of the gap between them defines the exciton binding energy E_{ex} in Fig. 2. In the metal phase we still see clearly visible Hubbard bands, at least up to the insulator spinodal line $U_{\text{cl}}(n)$ [15], now coexisting with a narrow quasiparticle peak at the Fermi energy. We mention that the persistence of excitonic absorption in the EHL above the Mott transition has been indeed observed experimentally [10, 29, 30].

Upon further increasing E_{ex} , or, equivalently, U , the Mott insulator becomes stable. However, the nature of the transition strongly depends on E_{ex} . Above a critical binding energy the transition is of second order and it coincides with the metal spinodal line (blue), in clear contrast with DMFT results, but it becomes first order for smaller binding energies, leading to a phase separation between a higher density EHL and a lower density Mott exciton insulator (Dark grey region in Fig. 2).

We cannot exclude that at finite temperature $T \neq 0$ a part of the second-order line becomes discontinuous as it happens at $n = 1$ [14] as a consequence of the larger entropy of the insulator. However, at fixed and large average magnetisation m , i.e., small n , it is not obvious to us that entropic considerations at $T \neq 0$ imply that a

Mott insulator at $m_{\text{I}} > m$ should prevail over a metal at $m_{\text{M}} < m$. We rather believe that a second order region survives at small n .

In summary, we have shown that an idealized model of photoexcited semiconductors yields a description of the exciton Mott transition in qualitative agreement with the experimental evidence of both first and second order transitions. We find that the discriminating factor is the magnitude of the exciton binding energy: for small E_{ex} the transition is discontinuous whereas it turns continuous for large E_{ex} . Also this result is compatible with the experimental framework. For instance, Mott transitions in bulk semiconductors [5, 7, 30, 31] are typically first order, while continuous transitions are observed in semiconductor quantum wells [9, 11, 12], consistently with their larger exciton binding energies due to spatial confinement.

This work has been supported by the European Union under H2020 Framework Programs, ERC Advanced Grant No. 692670 “FIRSTORM”. We thank Nicola Lanatà and Adriano Amaricci for useful discussions. D.G. thanks R. Raimondi for fruitful discussions.

-
- [1] W. F. Brinkman and T. M. Rice, Phys. Rev. B **7**, 1508 (1973), URL <https://link.aps.org/doi/10.1103/PhysRevB.7.1508>.
 - [2] N. F. Mott, Contemporary Physics **14**, 401 (1973), <https://doi.org/10.1080/00107517308210764>, URL <https://doi.org/10.1080/00107517308210764>.
 - [3] T. Rice (Academic Press, 1978), vol. 32 of *Solid State Physics*, pp. 1 – 86, URL <http://www.sciencedirect.com/science/article/pii/S0081194708604385>.
 - [4] N. F. Mott, Proceedings of the Physical Society. Section A **62**, 416 (1949), URL <http://stacks.iop.org/0370-1298/62/i=7/a=303>.
 - [5] L. M. Smith and J. P. Wolfe, Phys. Rev. Lett. **57**, 2314 (1986), URL <https://link.aps.org/doi/10.1103/PhysRevLett.57.2314>.
 - [6] A. H. Simon, S. J. Kirch, and J. P. Wolfe, Phys. Rev. B **46**, 10098 (1992), URL <https://link.aps.org/doi/10.1103/PhysRevB.46.10098>.
 - [7] M. Nagai, R. Shimano, K. Horiuchi, and M. Kuwata-Gonokami, Phys. Rev. B **68**, 081202 (2003), URL <https://link.aps.org/doi/10.1103/PhysRevB.68.081202>.
 - [8] M. Stern, V. Garmider, V. Umansky, and I. Bar-Joseph, Phys. Rev. Lett. **100**, 256402 (2008), URL <https://link.aps.org/doi/10.1103/PhysRevLett.100.256402>.
 - [9] L. Kappei, J. Szczytko, F. Morier-Genoud, and B. Deveaud, Phys. Rev. Lett. **94**, 147403 (2005), URL <https://link.aps.org/doi/10.1103/PhysRevLett.94.147403>.
 - [10] T. Suzuki and R. Shimano, Phys. Rev. Lett. **109**, 046402 (2012), URL <https://link.aps.org/doi/10.1103/PhysRevLett.109.046402>.
 - [11] G. Rossbach, J. Levrat, G. Jacopin, M. Shahmohammadi, J.-F. Carlin, J.-D. Ganière, R. Butté, B. Deveaud, and N. Grandjean, Phys. Rev. B **90**,

- 201308 (2014), URL <https://link.aps.org/doi/10.1103/PhysRevB.90.201308>.
- [12] G. Kiršanskė, P. Tighineanu, R. S. Daveau, J. Miguel-Sánchez, P. Lodahl, and S. Stobbe, *Phys. Rev. B* **94**, 155438 (2016), URL <https://link.aps.org/doi/10.1103/PhysRevB.94.155438>.
- [13] G. Wang, A. Chernikov, M. M. Glazov, T. F. Heinz, X. Marie, T. Amand, and B. Urbaszek, *Rev. Mod. Phys.* **90**, 021001 (2018), URL <https://link.aps.org/doi/10.1103/RevModPhys.90.021001>.
- [14] A. Georges, G. Kotliar, W. Krauth, and M. J. Rozenberg, *Rev. Mod. Phys.* **68**, 13 (1996).
- [15] G. Kotliar, *The European Physical Journal B - Condensed Matter and Complex Systems* **11**, 27 (1999), ISSN 1434-6036, URL <http://dx.doi.org/10.1007/s100510050914>.
- [16] P. Nozières and S. Schmitt-Rink, *Journal of Low Temperature Physics* **59**, 195 (1985), ISSN 1573-7357, URL <http://dx.doi.org/10.1007/BF00683774>.
- [17] L. Laloux, A. Georges, and W. Krauth, *Phys. Rev. B* **50**, 3092 (1994), URL <https://link.aps.org/doi/10.1103/PhysRevB.50.3092>.
- [18] M. Capone, C. Castellani, and M. Grilli, *Phys. Rev. Lett.* **88**, 126403 (2002), actually study the attractive case at fixed density, which, as mentioned in the text, is equivalent to the repulsive one at fixed magnetisation, URL <https://link.aps.org/doi/10.1103/PhysRevLett.88.126403>.
- [19] J. Bauer and A. C. Hewson, *Phys. Rev. B* **76**, 035118 (2007), URL <https://link.aps.org/doi/10.1103/PhysRevB.76.035118>.
- [20] W. Metzner and D. Vollhardt, *Phys. Rev. Lett.* **62**, 324 (1989), URL <http://link.aps.org/doi/10.1103/PhysRevLett.62.324>.
- [21] With a state $|\psi\rangle$ of finite magnetisation m we mean that the expectation value on such a state of the impurity spin operator \mathbf{S} along a given direction is m , whilst its projection vanishes in the perpendicular plane. Because of $SU(2)$ symmetry, for any direction there will be a corresponding equally legitimate state. In the text we choose for convenience the z -direction.
- [22] See Supplemental material.
- [23] N. Lanatà, T.-H. Lee, Y.-X. Yao, and V. Dobrosavljević, *Phys. Rev. B* **96**, 195126 (2017), URL <https://link.aps.org/doi/10.1103/PhysRevB.96.195126>.
- [24] S. Vitiello, K. Runge, and M. H. Kalos, *Phys. Rev. Lett.* **60**, 1970 (1988), URL <https://link.aps.org/doi/10.1103/PhysRevLett.60.1970>.
- [25] S. Rommer and S. Östlund, *Phys. Rev. B* **55**, 2164 (1997), URL <https://link.aps.org/doi/10.1103/PhysRevB.55.2164>.
- [26] R. Orús, *Annals of Physics* **349**, 117 (2014), ISSN 0003-4916, URL <http://www.sciencedirect.com/science/article/pii/S0003491614001596>.
- [27] G. Carleo and M. Troyer, *Science* **355**, 602 (2017), ISSN 0036-8075, URL <http://science.sciencemag.org/content/355/6325/602>.
- [28] N. Lanatà, Y. Yao, C.-Z. Wang, K.-M. Ho, and G. Kotliar, *Phys. Rev. X* **5**, 011008 (2015), URL <http://link.aps.org/doi/10.1103/PhysRevX.5.011008>.
- [29] P. Grivickas, V. Grivickas, and J. Linnros, *Phys. Rev. Lett.* **91**, 246401 (2003), URL <https://link.aps.org/doi/10.1103/PhysRevLett.91.246401>.
- [30] F. Sekiguchi, T. Mochizuki, C. Kim, H. Akiyama, L. N. Pfeiffer, K. W. West, and R. Shimano, *Phys. Rev. Lett.* **118**, 067401 (2017), URL <https://link.aps.org/doi/10.1103/PhysRevLett.118.067401>.
- [31] L. M. Smith and J. P. Wolfe, *Phys. Rev. B* **51**, 7521 (1995), URL <https://link.aps.org/doi/10.1103/PhysRevB.51.7521>.
-

Supplemental material: Exciton Mott transition revisited

1. THE VARIATIONAL g-GW TECHNIQUE

We shall consider the following tight-binding model on a lattice with coordination number z :

$$H = -\frac{1}{\sqrt{z}} \sum_{\langle ij \rangle} \sum_{a,b=1}^n \left(t_{ij}^{ab} d_{ia}^\dagger d_{jb} + h.c. \right) + \sum_i H_i \quad (1)$$

where d_{ia} annihilates an electron at site i in the spinful orbital $a = 1, \dots, n$, and H_i is a local term that accounts also for interactions. We look for the ground state of Hamiltonian (1) in the subspace of variational wavefunctions:

$$|\Psi\rangle = \prod_i \mathcal{P}_i |\Psi_*\rangle, \quad (2)$$

where $|\Psi_*\rangle$ is a generic Slater determinant for $N \geq 1$ spinful orbitals. Whereas,

$$\mathcal{P}_i = \sum_{\Gamma\gamma} \lambda_{\Gamma\gamma} |\Gamma_i\rangle \langle \gamma_i| \quad (3)$$

is a linear operator acting on site i and:

$$|\Gamma_i\rangle = \prod_{a=1}^n \left(d_{ia}^\dagger \right)^{n_a(\Gamma)} |0\rangle, \quad (4)$$

$$|\gamma_i\rangle = \prod_{\alpha=1}^N \left(c_{i\alpha}^\dagger \right)^{n_\alpha(\gamma)} |0\rangle. \quad (5)$$

Therefore, the local projector $|\Gamma_i\rangle \langle \gamma_i|$ maps a local N -auxiliary orbital configuration $|\gamma_i\rangle$ into a physical orbital one $|\Gamma_i\rangle$, and $\lambda_{\Gamma\gamma}$ are variational parameters. As shown in [1], there is a one to one correspondence between the matrix elements $\lambda_{\Gamma\gamma}$ and the components $\psi(\Gamma, \bar{\gamma})$, where $|\bar{\gamma}\rangle$ is the particle-hole transform of $|\gamma\rangle$, of a wavefunction:

$$|\psi\rangle = \sum_{\Gamma\bar{\gamma}} \psi(\Gamma, \bar{\gamma}) |\Gamma\rangle \times |\bar{\gamma}\rangle, \quad (6)$$

that describes an impurity coupled to a bath of N sites. By assuming translational invariance the average value of the energy reads

$$E[\psi] = \frac{1}{V} \langle \Psi_* | H_* | \Psi_* \rangle + \langle \psi | H_i | \psi \rangle, \quad (7)$$

where V is the number of sites, and H_i is the local term in the Hamiltonian acting on the impurity site. In Eq. (7) the Slater determinant Ψ_* is the ground-state of the non interacting Hamiltonian

$$H_* = -\frac{1}{\sqrt{z}} \sum_{\langle ij \rangle} \sum_{a,b=1}^n \sum_{\alpha,\beta=1}^N \left(c_{i\alpha}^\dagger R_{\alpha a}^\dagger t_{ij}^{ab} R_{b\beta} c_{j\beta} + h.c. \right) - \sum_i \sum_{\alpha,\beta=1}^N \left(\mu_{\alpha\beta} (c_{i\alpha}^\dagger c_{i\beta} - \Delta_{\alpha\beta}) \right), \quad (8)$$

where $\Delta_{\alpha\beta} = \langle \psi | c_\alpha c_\beta^\dagger | \psi \rangle$. In Eq. (8) the coefficients $R_{a\beta}$ are obtained by solving

$$\mathbf{Q}_a = \hat{S} \cdot \mathbf{R}_a, \quad (9)$$

where \mathbf{Q}_a has components $(\mathbf{Q}_a)_\alpha = \langle \psi | c_\alpha^\dagger d_a | \psi \rangle$, and the matrix $\hat{S} = \sqrt{\hat{\Delta} \cdot (1 - \hat{\Delta})}$. The single particle potential $\mu_{\alpha\beta}$ in Eq. (8) enforces the Gutzwiller constraints [1, 2]:

$$\langle \Psi_* | c_{i\alpha}^\dagger c_{i\beta} | \Psi_* \rangle = \Delta_{\alpha\beta} = \langle \psi | c_\alpha c_\beta^\dagger | \psi \rangle. \quad (10)$$

In summary the numerical implementation of the g-GW technique consists of the following steps:

- 1 Propose an impurity wavefunction $|\psi\rangle$.
- 2 Compute the bath's density matrix $\hat{\Delta}$ and the hybridisation vectors \mathbf{Q}_a .
- 3 Invert Eq. (9) for \mathbf{R}_a .
- 4 Solve the system of non-linear Eqs. (10) for the Lagrange multipliers $\mu_{\alpha\beta}$.
- 5 Compute the energy $E[\psi]$.
- 6 Check if the minimum is reached. Otherwise, go back to step 1.

2. g-GW APPLIED TO THE SINGLE BAND HUBBARD MODEL

We apply the g-GW technique, presented in section 1, to study the Mott transition in the single band Hubbard model both at zero and finite magnetisation.

For $U/2t \gg 1$ the bath's low energy level does not contribute to valence fluctuations on the impurity site. As discussed in the main text, it behaves as an isolated spin entangled with the remaining levels in a singlet configuration. Therefore, to describe the Mott transition in the magnetic sector we need at least $N = 3$ auxiliary orbitals, two of them, e.g. 1 the upper and 3 the lower, represent the Hubbard sidebands, while the third level is peaked at the Fermi level. At fixed magnetisation the energy functional $E[\psi]$ has to be minimised with respect to $|\psi\rangle$ subject to the constraint of half-filling and fixed magnetisation:

$$\langle\psi|n_{\uparrow} + n_{\downarrow}|\psi\rangle = 1, \quad \langle\psi|n_{\uparrow} - n_{\downarrow}|\psi\rangle = m. \quad (11)$$

Before introducing our results, we remind the reader the basic steps composing the g-GW variational technique. Given the variational wavefunction $|\psi\rangle$, which satisfies constraints (11), we compute the bath's density matrix:

$$\hat{\Delta}_{\sigma} = \begin{pmatrix} 1 - \langle c_{1\sigma}^{\dagger} c_{1\sigma} \rangle & -\langle c_{2\sigma}^{\dagger} c_{1\sigma} \rangle & -\langle c_{3\sigma}^{\dagger} c_{1\sigma} \rangle \\ -\langle c_{1\sigma}^{\dagger} c_{2\sigma} \rangle & 1 - \langle c_{2\sigma}^{\dagger} c_{2\sigma} \rangle & -\langle c_{3\sigma}^{\dagger} c_{2\sigma} \rangle \\ -\langle c_{1\sigma}^{\dagger} c_{3\sigma} \rangle & -\langle c_{2\sigma}^{\dagger} c_{3\sigma} \rangle & 1 - \langle c_{3\sigma}^{\dagger} c_{3\sigma} \rangle \end{pmatrix}, \quad (12)$$

where $\langle \dots \rangle = \langle \psi | \dots | \psi \rangle$ and

$$\mathbf{Q}_{\sigma} = \begin{pmatrix} \langle c_{1\sigma}^{\dagger} d_{\sigma} \rangle \\ \langle c_{2\sigma}^{\dagger} d_{\sigma} \rangle \\ \langle c_{3\sigma}^{\dagger} d_{\sigma} \rangle \end{pmatrix}, \quad \mathbf{R}_{\sigma} = \hat{S}_{\sigma}^{-1} \mathbf{Q}_{\sigma}, \quad (13)$$

where $\hat{S}_{\sigma} = \sqrt{\hat{\Delta}_{\sigma} \cdot (1 - \hat{\Delta}_{\sigma})}$. In the presence of a finite magnetisation the single particle potential is composed by six independent parameters:

$$\mu_{\sigma} = \begin{pmatrix} \mu_{1\sigma} & \mu_{12\sigma} & \mu_{13\sigma} \\ \mu_{12\sigma} & \mu_{2\sigma} & \mu_{23\sigma} \\ \mu_{13\sigma} & \mu_{23\sigma} & \mu_{3\sigma} \end{pmatrix}, \quad (14)$$

which are determined by solving Eq. (10). Finally, the energy can be computed:

$$E[\psi] = \frac{1}{V} \langle \Psi_* | H_* | \Psi_* \rangle + \langle \psi | n_{\uparrow} n_{\downarrow} | \psi \rangle. \quad (15)$$

The Mott transition in the paramagnetic sector

As discussed in the main text, g-GW technique displays coexistence between metallic and Mott insulating solution. Analogously with DMFT, it is possible to estimate the spinodal values of the interaction for the metal and the Mott insulator. In particular we found that $U_{c1} \simeq 1.85$ and $U_{c2} \simeq 2.88$. The evolution of the quasiparticle parameters $R_{\alpha\sigma}$ and $\mu_{\alpha\beta}$, defined in Eqs. (13) and (14), is shown in Fig. 1. We notice that in the paramagnetic case \mathbf{R}_{σ} and μ_{σ} are spin independent. Finally, in Fig. 2 we show the total energy E of the stable metal (red) and metastable insulator (blue), also in comparison with DMFT data using exact diagonalization with 7 bath levels instead of the 3 in the g-GW.

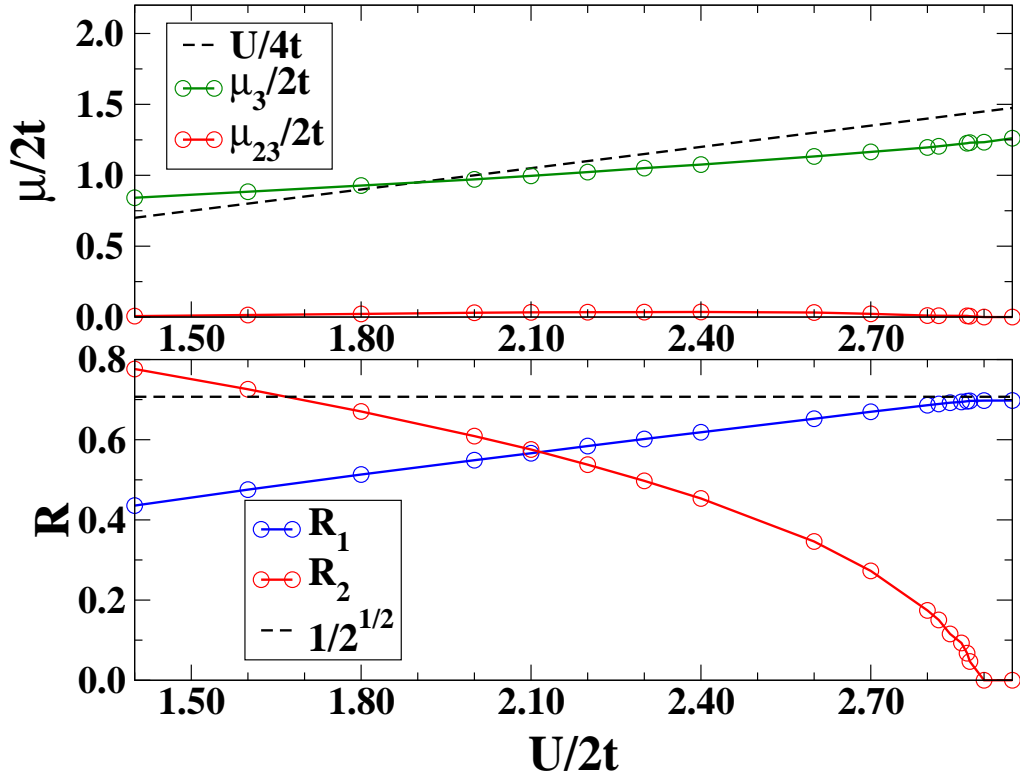


FIG. 1: Top: green and red lines correspond to components μ_3 and μ_{23} of Eq. (14) as a function $U/2t$. We notice that in the paramagnetic case $\mu_1 = -\mu_3$, $\mu_{12} = -\mu_{23}$ and $\mu_{13} = 0$. Black dashed line is $U/4t$, which corresponds to the large U limit of μ_3 in the Mott regime. Bottom: in blue and red we plot R_1 and R_2 , respectively, as a function of $U/2t$. Here, black dashed line is the asymptotic value assumed by R_1 in the Mott regime. We notice that in the paramagnetic case $R_1 = R_3$.

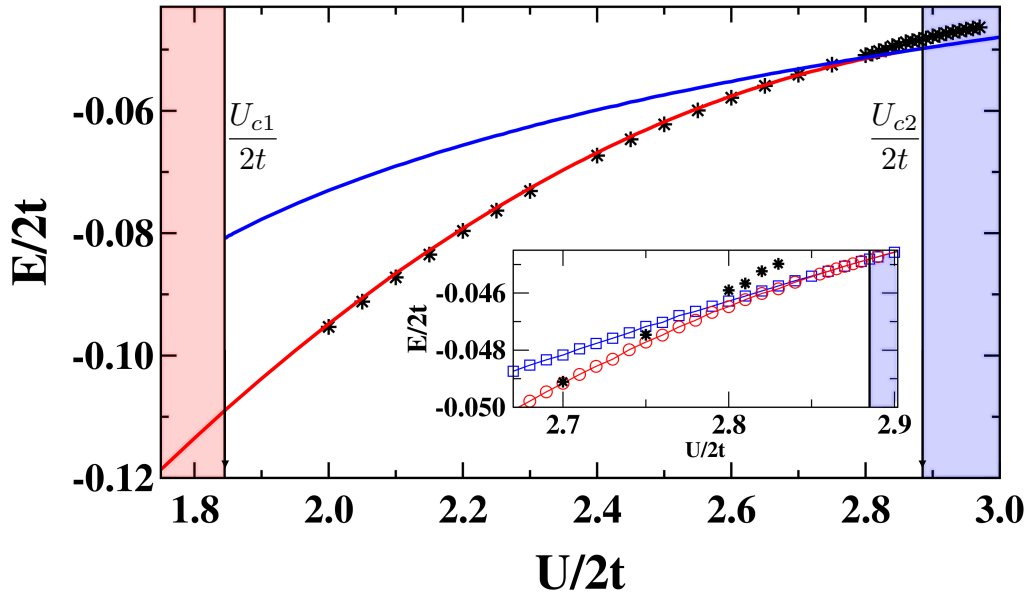


FIG. 2: We plot as function of $U/2t$ in red and blue the total energy E of the stable metal and metastable insulator, respectively. The starred symbols are obtained by DMFT with 7 bath levels instead of the 3 as in the variational g-GW. In the light red region only the metallic solution exists, while in the blue one the system is a Mott insulator.

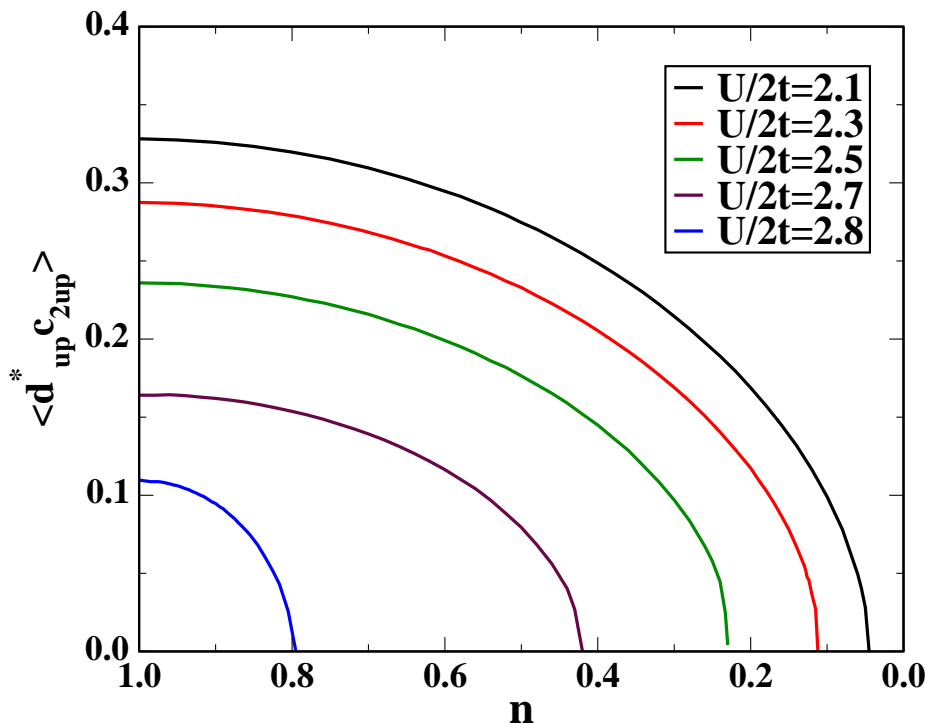


FIG. 3: We plot the expectation value $\langle d_{\sigma}^{\dagger} c_{2\sigma} \rangle$ of the hybridisation between the impurity and the level 2 as a function of m for several values of $U/2t$.

The Mott transition at finite magnetisation

In this section we study the Mott transition at finite magnetisation by applying the computational scheme outlined in section 2.

Results of the energy and double occupancy as a function of the magnetisation are shown in Figs. 4 and 5. Instead, in Fig. 3 we present the evolution of $\langle \psi | d_{\sigma}^{\dagger} c_{2\sigma} | \psi \rangle$, which plays the role of the order parameter for the Mott transition. Finally, in Fig. 6 we show the energy and its first order derivative as a function of the magnetisation. At a critical value of the magnetisation the metallic solution becomes unstable and phase separation between the metal and the insulator occurs. As shown in the (U, m) phase diagram, there is a critical value of the interaction above which no phase separation occurs. In Fig. 7 we show the energy and its first order derivative as a function of the magnetisation for $U/2t = 2.5$. In this case no phase separation is observed.

3. DYNAMICAL MEAN-FIELD THEORY'S RESULTS

In this section we briefly report the results obtained by using dynamical mean-field theory (DMFT) with exact diagonalisation impurity solver. We consider the Hamiltonian:

$$H = -\frac{t}{\sqrt{z}} \sum_{\langle ij \rangle} \sum_{\sigma} \left(d_{i\sigma}^{\dagger} d_{j\sigma} + h.c. \right) + U \sum_i n_{i\uparrow} n_{i\downarrow} - h \sum_i (n_{i\uparrow} - n_{i\downarrow}), \quad (16)$$

on a Bethe's lattice with coordination number z . In Eq. (16) t is the hopping amplitude between nearest-neighbor sites, U is the on-site interaction, h is the Zeeman splitting term. We look for the DMFT solution of (16) in the half-filled sector: $\langle n_i \rangle = 1$. The phase diagram (h, U) obtained is shown in the left picture of Fig. 8. As discussed in the main text, zero temperature DMFT calculations are not able to converge to a partially polarised Mott insulator. Indeed, in the presence of a charge gap any infinitesimal Zeeman field induces full polarisation of the impurity spin, which translates into full spin polarisation of the lattice model. Top right picture in Fig. 8 shows that the instability of the impurity model indeed results into a first order transition between a partially polarised metal and a fully polarised band insulator.

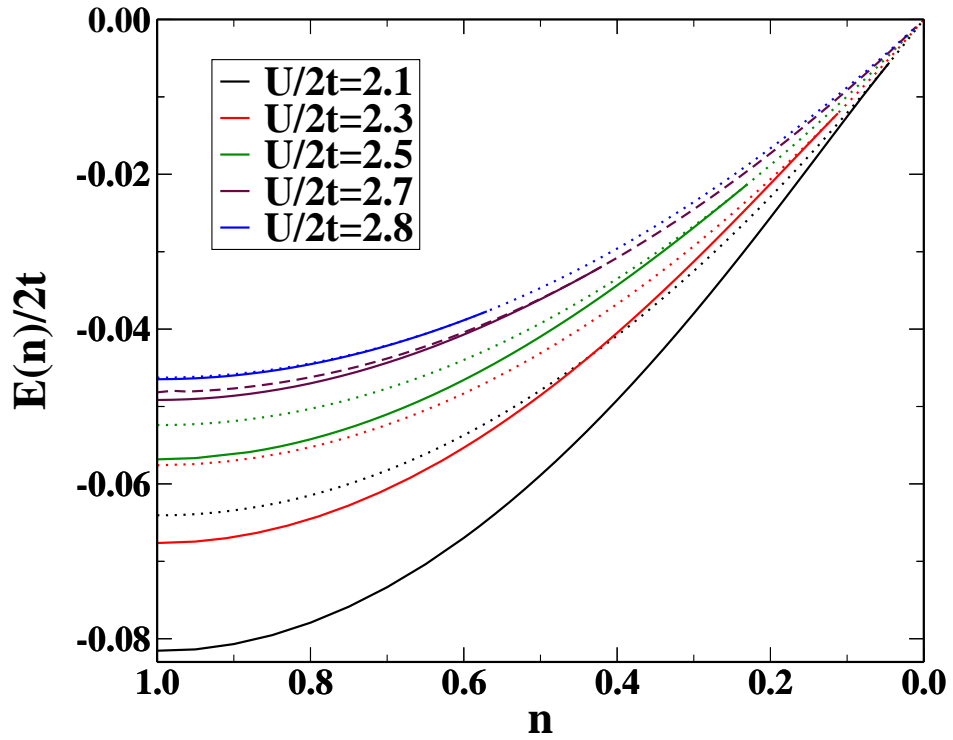


FIG. 4: We compare the energy of the metal and Mott insulator in the coexistence region. In particular, in solid lines we plot the total energy as a function of the magnetisation, while in dashed lines we draw the energy of the Mott insulating solution.

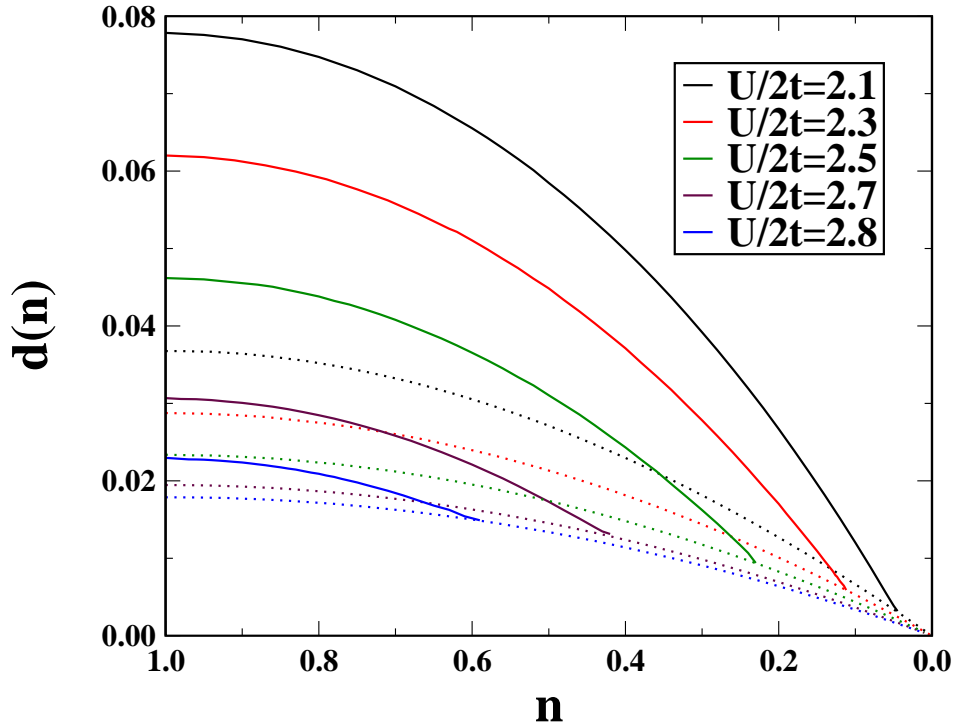


FIG. 5: Comparison between $\langle n_{\uparrow}n_{\downarrow} \rangle$ of the metal and Mott insulator in the coexistence region. In particular, in solid lines we plot the double occupancy as a function of the magnetisation, while in dashed lines we draw the double occupancy of the Mott insulating solution.

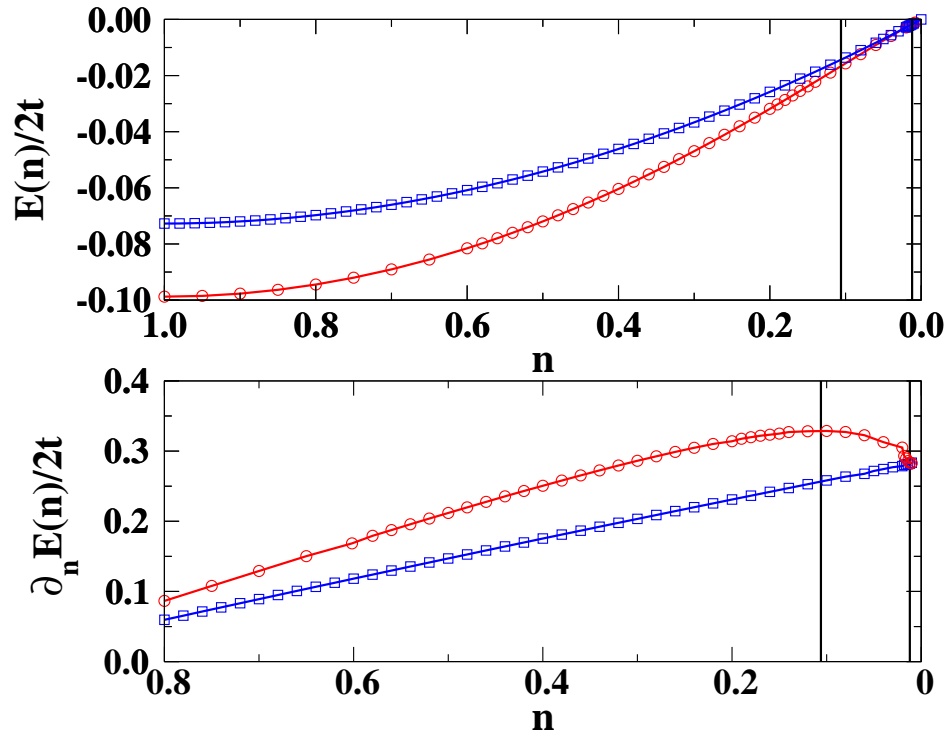


FIG. 6: Energy and first order derivative of the variational energy as a function of the magnetisation for $U/2t = 1.9$. Red data refer to the metal, while blue ones to the Mott insulator. Above a critical magnetisation, signalled by the first vertical black line, the metal becomes unstable. Eventually, at the second vertical line, the metallic solution merges continuously in the Mott insulator.

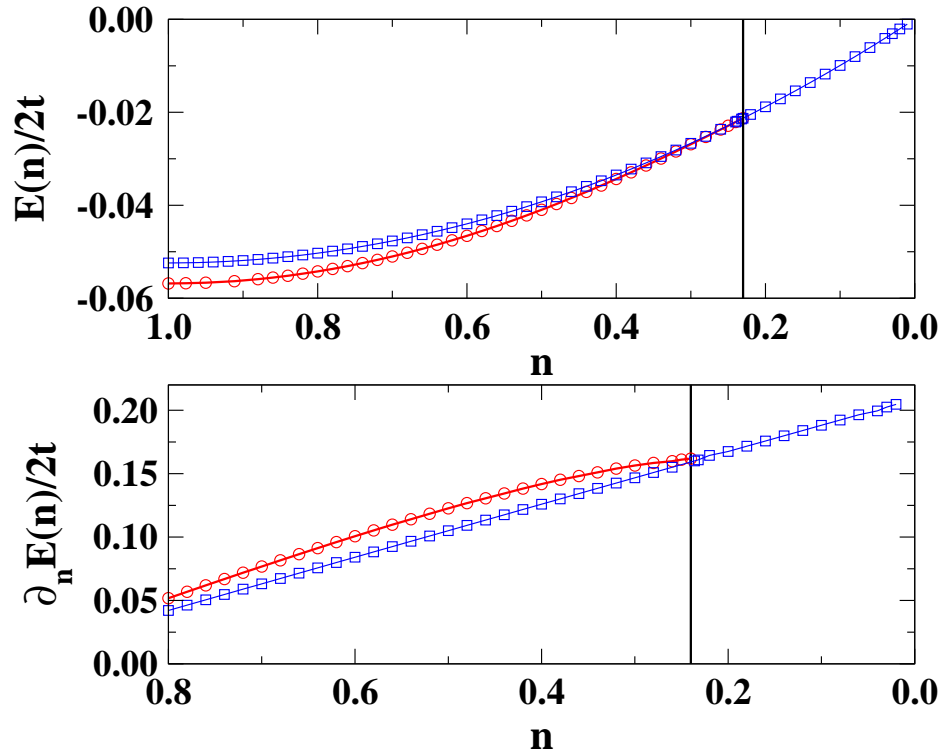


FIG. 7: Energy and first order derivative of the variational energy as a function of the magnetisation for $U/2t = 2.5$. Red data refer to the metal, while blue ones to the Mott insulator. The metallic solution is stable as a function of the magnetisation. Eventually, signalled by the vertical black line, the metallic solution merges continuously in the Mott insulator.

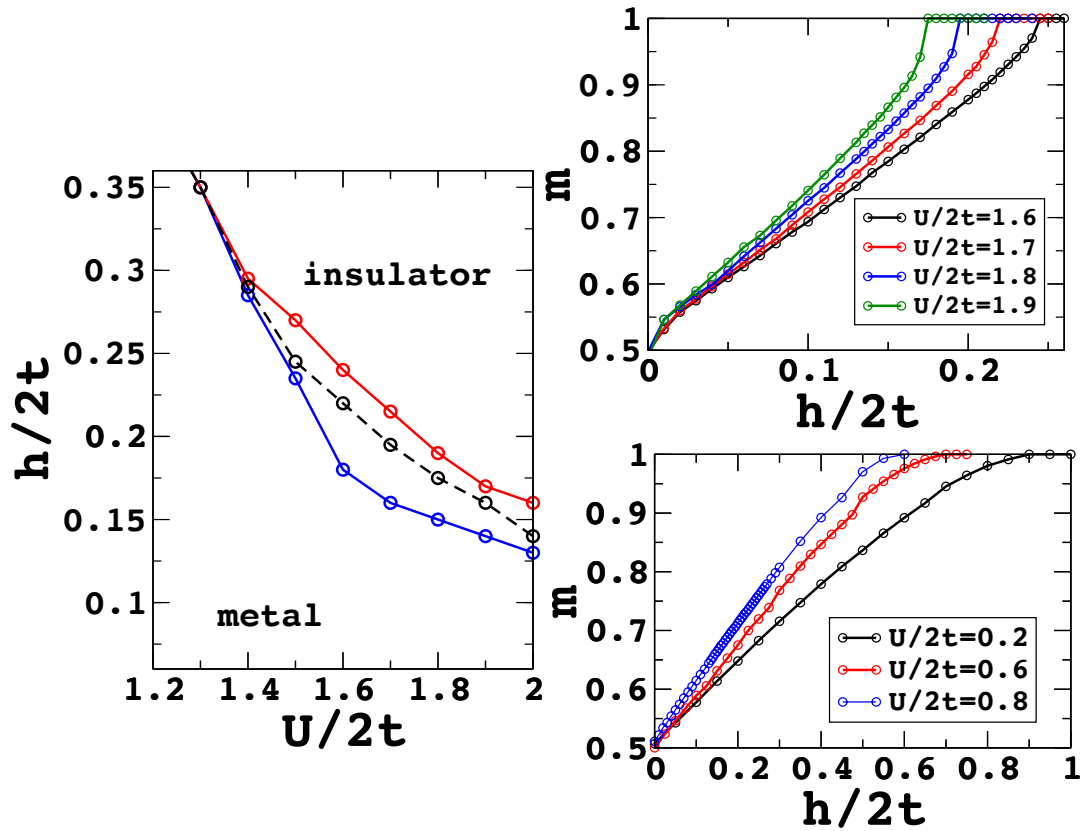


FIG. 8: Left: in blue we plot the spinodal line of the insulating solution, while in red the spinodal line of the metal. Black dashed line represents the critical Zeeman field where the energy crossing between metal and insulator occurs. Right: magnetisation as a function of the applied magnetic field for several values of the external field.

-
- [1] Nicola Lanatà, Yongxin Yao, Cai-Zhuang Wang, Kai-Ming Ho, and Gabriel Kotliar. Phase diagram and electronic structure of praseodymium and plutonium. *Phys. Rev. X*, 5:011008, Jan 2015.
- [2] Michele Fabrizio. The out-of-equilibrium time-dependent gutzwiller approximation. In Veljko Zlatic and Alex Hewson, editors, *New Materials for Thermoelectric Applications: Theory and Experiment*, NATO Science for Peace and Security Series B: Physics and Biophysics, pages 247–273. Springer Netherlands, 2013.